Shape Deposition Manufacturing of a Soft, Atraumatic, Deployable Surgical Grasper

Joshua Gafford[1], Ye Ding[1], Andrew Harris[1], Terrence McKenna[1], Panagiotis Polygerinos[1], Dónal Holland[1], Conor Walsh[1,2,*]
[1]Harvard University School of Engineering and Applied Sciences
[2]Wyss Institute for Biologically-Inspired Engineering
Cambridge, MA 02138
*Corresponding Author, Email: walsh@seas.harvard.edu

Arthur Moser[3]
Department of Surgery
[3]Beth Israel Deaconess Medical Center
330 Brookline Avenue, Boston, MA 02215

This paper details the design, analysis, fabrication and validation of a deployable, atraumatic grasper intended for retraction and manipulation tasks in manual and robotic minimally-invasive surgical procedures. Fabricated using a combination of shape deposition manufacturing (SDM) and 3D printing, the device (which acts as a deployable end-effector for robotic platforms) has the potential to reduce the risk of intraoperative hemorrhage by providing a soft, compliant interface between delicate tissue structures and the metal laparoscopic forceps and graspers that are currently used to manipulate and retract these structures on an ad-hoc basis. This paper introduces a general analytical framework for designing SDM fingers where the desire is to predict the shape and the transmission ratio, and this framework was used to design a multi-jointed grasper that relies on geometric trapping to manipulate tissue, rather than friction or pinching, to provide a safe, stable, adaptive and conformable means for manipulation. Passive structural compliance, coupled with active grip force monitoring enabled by embedded pressure sensors, helps to reduce the cognitive load on the surgeon. Initial manipulation tasks in a simulated environment have demonstrated that the device can be deployed though a 15mm trocar and develop a stable grasp using Intuitive Surgical's daVinci robotic platform to deftly manipulate a tissue analog.

1 Introduction

Laparoscopic surgery is a minimally invasive surgical (MIS) technique that involves making multiple small incisions (generally between 3mm and 15mm wide) in a patient's abdomen. Due to the size limitations imposed by MIS, current laparoscopic tools used to retract or manipulate delicate
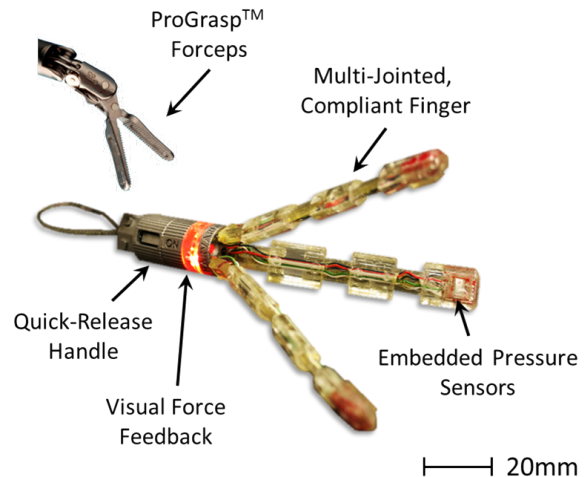

Fig. 1. Deployable manipulator prototype, with daVinci ProGrasp forceps for scale. When closed, the device has a diameter of 14mm and a length of 96mm. When open, the diameter of the finger tips is 86mm, resulting in an encompassed volume of 116 cm^3

tissues are morphologically simple in nature, with fulcrum-based, rigid, steel components incapable of sufficiently distributing forces (imagine using needle-nose pliers to pick up a water balloon). Especially in robotic surgery where haptic feedback is lost, this often leads to tissue damage and inadvertent perforation of thin-walled, high-pressure vessels which can lead to fluid leakage and hemorrhage [1].

As current conventional manufacturing approaches are ill-suited and cost-ineffective at fabricating sensorized, dexterous devices at the scales required, we must look towards alternative materials and manufacturing approaches to develop a suite of atraumatic tools that provide inherently safe
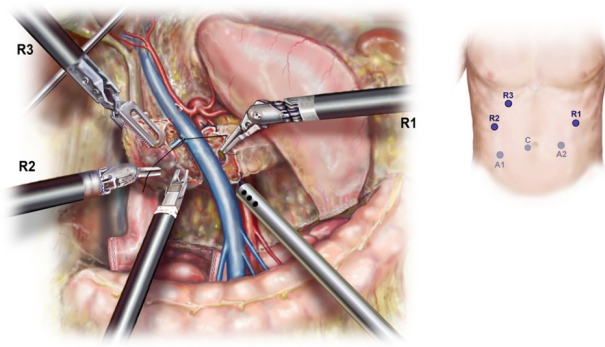
Fig. 2. (left) Artist's rendition of robotic pancreaticoduodenectomy, where the pancreas, SMV and SMA are shown, (right) port placement (reprinted with permission from Elsevier) [1]

interactions with delicate anatomy. To deviate away from the rigid metal tools that are currently used to manipulate sensitive anatomy on an ad-hoc basis, we employed a technique called shape deposition manufacturing (SDM) [2–4] to fabricate a soft, compliant and dexterous manipulator with force distribution capabilities for tissue manipulation and retraction in MIS procedures (see Fig. 1). Polymer-based multi-jointed fingers with embedded pressure sensors and actuation cabling were fabricated in a monolithic molding process, obviating the need for post-fabrication assembly of individual components. In addition, embedded pressure sensors continuously monitor the grasping force and relay this information back to the surgeon via a bright LED ring that changes color once a pressure threshold (defined pre-operatively) has been exceeded. The grasping mechanism itself utilizes both geometric trapping as well as frictional forces to eliminate stress concentrators and reduce the likelihood of tissue and vessel damage for a passively- and actively-safe interface between rigid forceps and delicate tissue.

The grasper presented herein has potential applicability in a number of minimally-invasive laparoscopic and robot-assisted laparoscopic procedures. To constrain the possible design space, we targeted tissue manipulation and retraction in robotic pancreaticoduodenectomy and considered the procedure-specific limitations thereof to develop functional requirements for the device.

1.1 The Robotic Pancreaticoduodenectomy

Of the advanced procedures performed laparoscopically, gastrointestinal (GI) surgery in general is seeing a marked paradigm shift from open to minimally-invasive as tools become smarter and more sophisticated. One of the most difficult laparoscopic GI operations is the pancreatico-duodenectomy, commonly known as the Whipple procedure, due to its inherent complexity and associated morbidity [5]. A Whipple procedure is performed to remove cancerous tissue from the head of the pancreas, and can be performed robotically using Intuitive Surgical's *daVinci* teleoperative robotic platform (Intuitive Surgical, Sunnyvale, CA).

The proximity of several high-pressure vessels (most notably, the superior mesenteric artery (SMA), superior mesen-

teric vein (SMV) and the portal vein as shown in Fig. 2), as well as the delicate nature of the pancreas itself, makes the Whipple procedure extremely prone to intraoperative complications via vessel puncture or leakage [1]. Any amount of bleeding or leakage can obfuscate the surgeon's view of the workspace, thus complicating an already taxing procedure. If the hemorrhage is not adequately controlled in a timely manner, the surgeon is forced to convert the procedure to an open surgery.

In particular, manipulating the pancreas and locating the surrounding vasculature without damaging these structures remains challenging given the tools available to surgeons today. While the recent rise in the use of surgical robotic tools has helped to mitigate some of the difficulties associated with pancreatic MIS by providing multi-degree-of-freedom end effectors, these tools remain similar in form factor to existing manual laparoscopic tools [6, 7]. Thus, there is an opportunity to leverage the technical advantages of gastrointestinal robotic surgery and develop specific task-oriented tools that are optimized to handle large, delicate organs and tissues in an inherently safe manner.

1.2 Prior Art

Current laparoscopic graspers can be grouped into three broad categories: planar graspers, geometric graspers, and suction-based graspers. Planar graspers account for a majority of laparoscopic graspers currently in use and all of the laparoscopic graspers available for the *daVinci* Surgical System [8]. They use metal jaws (often serrated) to firmly compress tissue and generate high frictional forces to allow for manipulation. In general these graspers are designed to perform highly skilled, dexterous tasks (such as tying sutures) in limited workspaces and are not necessarily optimized for handling large organs or swaths of tissue for retraction or general manipulation purposes. Planar graspers operate by pinching tissue and, as a result, are generally ineffective at handling larger structures like whole organs. In addition, these tools are often sharp and easily puncture tissue and vessels. Geometric graspers attempt to trap sections of tissue to allow for safer manipulation, akin to a human hand holding a water balloon, where the overall grasping force is small and distributed over a large area. However, current devices are not soft and are often complex to control and as such are rarely found in common use in hospitals today aside from stationary retractors. Furthermore, all geometric graspers reviewed by the authors had to be controlled manually [9–13]. Currently, the majority of suction-based graspers that have found widespread use are not adapted for MIS [14]. Some patents exist for suction-assisted planar graspers but such designs have not penetrated the commercial market [15]. Given the current device landscape, there is an opportunity to innovate in this space and employ integrated manufacturing techniques to develop a suite of highly dexterous and conformable tools specifically designed to manipulate large, delicate anatomy.

Deploy through 15mm trocar | Retrieve with laparoscopic forceps | Tighten around tissue until LED turns red
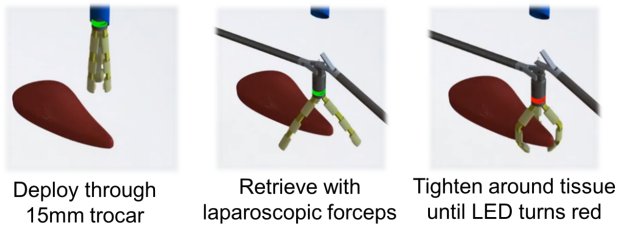
Fig. 3. Procedural workflow of deployable atraumatic grasper, where two forceps are used to position and actuate the device. After the device has been deployed, only one forcep is required for additional retraction tasks
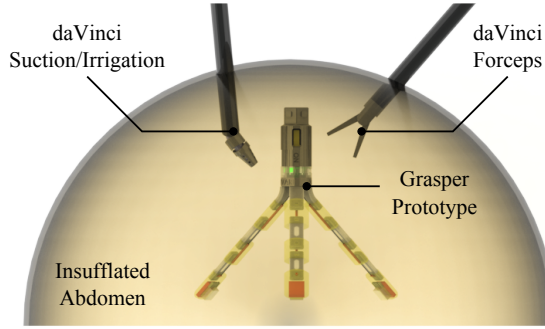

Fig. 4. Grasper prototype mapped against a rendering of an insufflated abdomen. daVinci tools provide reference

1.3 Contribution

The aim of this work is to demonstrate the applicability of shape deposition manufacturing to the development of 'soft' medical devices where compliance, conformability and dexterity are paramount. In addition, we aim to provide a general analytical framework for designing and optimizing systems which incorporate integrated manufacturing techniques, and demonstrate this framework in the design and optimization of a pressure-sensitive grasper with task-specific clinical applicability.

The proposed analytical framework was used to design and fabricate a soft, deployable grasper that is compatible with the current clinical workflow, using a standard trocar size for insertion and removal, and can be operated by commercially available manual and robotic laparoscopic instruments as shown in Fig. 3. The grasping mechanism itself utilizes geometric trapping in addition to friction to distribute grasping forces and manipulate tissue within safe stress thresholds [16] which, coupled with integrated pressure sensing, reduces the likelihood of tissue and vessel damage. Our device augments the capabilities already offered by robotic laparoscopic tools (namely, multiple-DOF intracorporeal dexterity) to realize an untethered, pressure-sensing end-effector that is adaptable, compliant and dexterous for large-organ retraction tasks in an insufflated abdomen, as shown in Fig. 4.

2 Design and Manufacturing

In order to seamlessly integrate into the current clinical workflow, the design must meet a number of conditions specific to size, ergonomics, and function. For example, the largest trocar port used during a Whipple procedure is a

Table 1. Functional Requirements

Category	Requirement	Value
Ergonomics	Diameter	<15mm
	Length	< 12 cm
	Setup Time	<5 min
	Removal Time	<30 sec
	Setup Tools	2 ProGrasp
	Retraction Tools	1 ProGrasp
Function	Max Load	>200 grams
	Encompassed Volume	>75 cm^3
	Actuation Force	<10 N
	Passive State	Open
Morphology	Distribute Force	N/A
	Soft Materials	N/A
	Biocompatible	N/A
	Sterilizable	N/A

15mm port for retraction tools, so this limitation sets an upper bound on our device diameter. It must be strong enough to lift an average adult pancreas (mean weight: 91.8g [17]) against gravity, and open up wide enough to encompass the volume of an average adult pancreas (72.7 ± 4.5 cm^3 [18]). The device must be small enough to be maneuverable inside an insufflated abdomen (given an insufflation volume of $V = 0.004m^3$ [19], and modeling the abdomen as a hemisphere, we can solve for the maximum grasper length l: $l < \sqrt[3]{(3V)/2\pi)}$). In addition, the device must be easy to actuate, manipulate, and retract using the current *daVinci* toolset. The device must be 'inherently soft', in that its form factor and constituent materials must not pose a puncture threat to soft tissue and vasculature. Finally, the constituent materials of the device must be biocompatible and sterilizable.

Several visits to the operating room, Whipple procedure observations, and consultations with expert robotic pancreatic surgeons further contributed to understanding the clinical environment and desired functional requirements, which are summarized in Table 1.

2.1 Device Design

The design of the cable-driven multi-jointed manipulator was driven by the aforementioned functional requirements, as well as the intended fabrication process. Shape Deposition Manufacturing (SDM) was identified as the optimal fabrication approach for the multi-jointed fingers given the functional requirements, as well as the ease of embed-
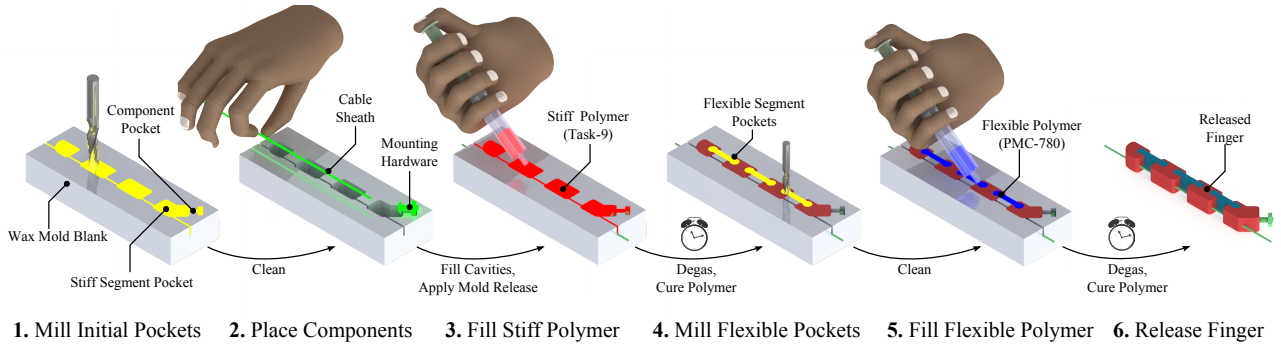
Fig. 5. Shape deposition process used in the fabrication of empirical finger models. Yellow indicates a subtractive step, green indicates pick-and-placement, red indicates a stiff polymer additive step, and blue indicates a flexible polymer additive step

ding discrete components (such as sensors and cables) and pre-programming the kinematic profile based on the geometry and material heterogeneity.

2.2 Shape Deposition Manufacturing

In addition to the novelty of leveraging current robot-assisted laparoscopic capabilities by developing a tool that can be deployed and manipulated in vivo, the primary contribution of this work is the use of a shape deposition manufacturing technique to fabricate the pressure-sensitive fingers (the specifics of which are discussed and analyzed in subsequent sections) [2–4]. SDM is beneficial for our application due to soft constituent materials (urethane-based plastics and rubbers), implicit encapsulation and isolation of sensors/wiring/cabling from the environment, and automatic strain relief, as the sensor, leads and wires are hard-molded into a stiff polymer structure. In addition, manufacturing and assembly are combined into a single step, resulting in process efficiency. The technique has been demonstrated as a means of manufacturing robust and adaptive robotic hands [20] and biomimetic mechanisms [21], and as such, we identified the opportunity to expand the technique to develop dexterous, compliant and conformable medical devices.

The basic planar SDM process, illustrated in Fig. 5, consists of a series of additive and subtractive manufacturing steps used to mold a heterogeneous, monolithic mechanism with spatially-varying and arbitrarily-selectable stiffness and geometric properties. By placing various components in the mold prior to pouring, automatic positioning and encapsulation of sensors, actuators and mounting hardware can be achieved. The flexibility to arbitrarily select joint stiffnesses and geometries allows a designer to customize the finger's deformed shape upon actuation, and as such, it is important to be able to predict such behavior pre-manufacturing. In the next section, we present the development of simple deterministic design tools for approximating and optimizing the kinematic behavior of different finger geometries prior to fabrication. We use the open-mold SDM process depicted in Fig. 5 to quickly prototype empirical fingers for model validation and optimization. We then use a more involved closed-top SDM process to implement the optimized the design into a form-factor compatible with our clinically-derived functional requirements.

2.3 Multi-Jointed Finger Design

A three finger design where fingers mutually oppose each-other at a 120 degree angle was selected to allow for a high surface area for each finger to better distribute grasping force and enable a grasped object to be completely constrained. This configuration also has the advantage of maximizing the surface area and volume of each finger given the 15mm diameter size constraint. Each finger has 3 joints, a design decision motivated by analyses explained in subsequent sections.

2.3.1 Analytical Modeling and Optimization

In order to minimize the number of manufacturing iterations and better understand the kinematics of a flexure-based multi-jointed finger fabricated via SDM, a mathematical model of a cable-driven, compliant finger was created in MATLAB (Nattick, MA) to analytically determine the distal deflection, transmission ratio (the ratio between the input tension force and output force applied by the distal segment) and overall deformed shape for any arbitrary finger configuration. Unlike simple pin-joint-based serial kinematic chains which typically describe discrete-component multi-jointed fingers, the monolithic, flexural nature of the SDM fingers requires a model of the flexural mechanics coupled with a kinematics model to accurately describe finger behavior. Note that a high-fidelity model is presented by Odhner and Dollar which uses Legendre polynomials to model flexure curvature and takes into account the secondary effects of stiffness and buckling, and as such, should be consulted if utmost accuracy is required [22]. The design tool presented herein, based on first principles, is simpler in nature and was used to quickly iterate and optimize designs, as well as to predict finger performance and deformation behavior a priori.

An illustration of a tendon-driven finger with a single flexible joint and rigid segment (showing all relevant dimensions) is shown in Fig. 6. A single joint-segment consists of a rigid section (subscript $i \in \{2, 3, ..., 2N\}$) and a flexible section (subscript $i-1$), and multiple joint-segments can be chained in series to obtain greater dexterity. The linear mechanics model assumes that the deformation is dominated by an applied moment at the distal segment of the finger and contributions from gravity, internal shear, and reaction forces in the x-direction are negligible. We can determine the over-
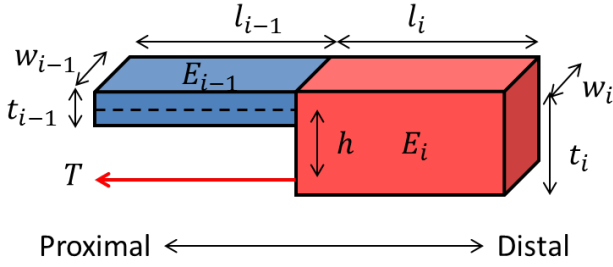
Fig. 6. Geometric and material parameters of a single segment, consisting of a flexible joint $(i-1)$ and stiff segment (i)

all deflection at the distal end of the finger by propagating internal moments created by the cable tension back to the proximal end and defining a global displacement with respect to the origin of the proximal-most segment (the global origin). Let us define a point $p_i(\delta_i, l_i)$ describing the position and orientation of section i, where δ_i denotes the local deflection between section i and section $i-1$ and l_i is the section length. Let us also define the orientation of section i as θ_i which denotes the angle between section i and section $i-1$. Static equilibrium holds that, in the absence of external forces, all internal distal moments caused by cable tension must be counter-balanced by equal and opposite proximal moments. Given a moment at the distal end of the section resulting from cable tensioning, and a fixed support boundary condition at the proximal end, we can use Castigliano's theorem to invoke an imaginary force Q at the junction between segments and superimpose this with the actuation cable moment $T_{h,i}$ to solve for the distal deflection and slope of the segment [23][1]:

$$\delta_i = \left. \frac{\partial U}{\partial Q} \right|_{Q=0}$$
$$= \int_0^{l_i} \frac{-Th_i + Qx}{E_i I_i} \left(\frac{\partial(-Th_i + Qx)}{\partial Q} \right) dx \Big|_{Q=0} \quad (1)$$

$$\delta_i = \frac{-Thl_i^2}{2E_i I_i} \quad (2)$$

$$\theta_i = \frac{\partial}{\partial x} \left(\left. \frac{\partial U}{\partial Q} \right|_{Q=0} \right) \Big|_{x=l_i} = \frac{-Th_i l_l}{E_i I_i} \quad (3)$$

Here, U is the strain energy of the segment, E_i is the effective Young's modulus, I_i is the second moment of area, l_i is the length of the segment and h_i is the distance between the neutral axis and the cable tension vector of the ith section[2]. Using Castigliano's theorem allows us to generalize

_____

[1] This mechanical model is a linear simplification used to quickly compare different finger geometries and their resulting deformed shape under loading. E_i is an 'effective modulus' that was obtained by comparing the model to empirical behavior of the urethane-based rubber joints. The accuracy of this linear model compared to hyperelastic models (such as Yeoh [24]) warrants further investigation and analysis.

[2] The cable actuation force is treated as a point load on the distal-most segment

Cable Configuration 1: Direct-Through
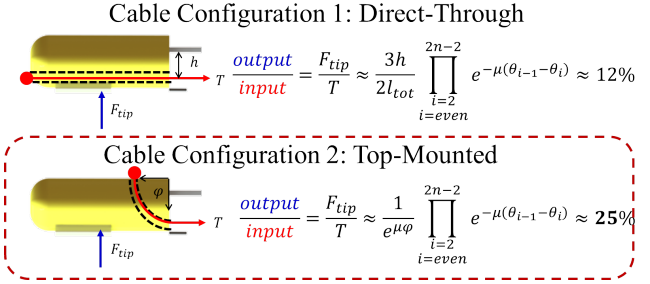

Cable Configuration 2: Top-Mounted

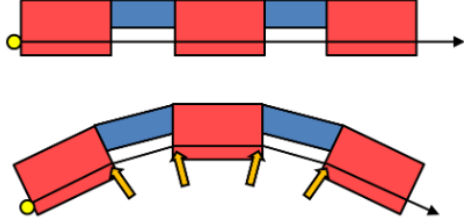Fig. 7. Cable orientation schemes and their resultant transmission ratio.

Fig. 8. Parasitic cable friction effects as the finger assumes a curved or actuated profile

Q for each segment, meaning we can solve for the deflection of any segment in the kinematic chain due to the distal moment resulting from cable tension. Note that the model has also been generalized to account for variable geometric and material properties.

Given the mechanics model presented above, we wish to construct a kinematics model for n flexible joints and n rigid segments (for simplicity, we assume an equal number of flexible joints and rigid segments) by establishing a global frame of reference $\{A\}$ at the proximal most joint and 'transforming' local deflections into the global frame. For brevity, this transformation is left to the appendices.

SDM offers the opportunity to arbitrarily select the actuating cable routing configuration. As such, it is important to note that the moment generated by cable tension, as well as the reaction force at the distal end of the finger, is dependent on the cable routing and termination scheme. We consider two cases as depicted in Fig. 7. A direct-through mounting scheme (top) results in a pure moment about the flexural joints, as the tension vector is in-line with the axis of the finger. A top mounted scheme (bottom) results in a capstan-like effect dependent on contact angle ϕ, as the tension vector is now perpendicular to the finger axis.

For the direct-through scheme, consider a simplified fixed-end cantilever model with a pure moment applied about the free end. The reaction force at the proximal end of the beam is denoted $R_{o,y}$ and is generated by the applied moment $M_o = Th$. In addition to solving this statically-indeterminant problem, we can add fidelity by approximating the 'parasitic capstan' effects that take place between the cable and the stiff segments as the finger assumes a curved profile (Fig. 8). As the segments lose colinearity during actuation, the cable imparts a reaction force that resists further actuation. To model

this, we have assumed a simple capstan relationship where the reaction force is dependent on the angle between subsequent stiff sections $(\theta_{i-1} - \theta_i)$. The cable is unconstrained as it passes through the flexible joints, and as such, we only consider parasitic capstan effects as the cable passes through the stiff segments. By taking this into account, the distal reaction force can be computed as follows:

$$R_{o,y} = \frac{3Th}{2\sum_{i=1}^{2n} l_i} \prod_{i=2,even}^{2n-2} e^{\mu(\theta_{i-1}-\theta_i)} \tag{4}$$

For the top-mounting scheme, the reaction force is modeled by the capstan equation, which is reproduced below:

$$R_{o,y} = \frac{T}{e^{\mu\phi}} \prod_{i=2,even}^{2n-2} e^{\mu(\theta_{i-1}-\theta_i)} \tag{5}$$

Here, ϕ is the contact angle and μ is the coefficient of static friction between the cable and the sheath (taken as 0.6 for a steel cable on polyurethane).

It should be noted that the modeling efforts presented here describe reaction force on the distal-most segment as a function of cable tension, as it is assumed (based on the application) that the distal segments would bear the majority of the load when retracting an organ against gravity. This analysis was meant to give a first-order approximation of the grasper's force application capabilities based on the cable mounting modality and is by no means a rigorous derivation of forces (1) at different points along the finger (i.e. proximal segments) and (2) throughout the bending motion. This level of detail is considered beyond the scope of the work presented herein and is a subject of future analysis.

2.3.2 Model Validation

To validate the numerical model kinematics, as well as to optimize the joint length and stiffness profile via an empirical comparative study, several finger model configurations were fabricated using the simple planar SDM process shown in Fig. 5. Following this process allowed for swift iteration and empirical optimization, allowing us to test various finger configurations which varied in terms of joint stiffness, number of joints, and link lengths. Using Task-9™ polyurethane (Smooth-On, Easton, PA) as the stiff segment material, PMC-780™ urethane rubber (Smooth-On) as the flexible segment material, several finger configurations were fabricated as shown in Fig. 9. The top three configurations, with direct-through mounting schemes, are listed below (where the stiffness of each flexible joint is spatially varied, and the stiffness magnitude is represented by a number from 1 to 3):

1. 3-jointed, proportional stiffness (3-2-1 proximal-distal)
2. 3-jointed, constant stiffness (3-3-3 proximal-distal)
3. 3-jointed, centrally flexible (3-1-2 proximal-distal)

Fig. 10 shows that the model kinematics closely match those of the fabricated prototypes for 2.5N actuation load. In addition, Table 2 shows each configuration's efficacy rating with respect to theoretical and measured transmission ratio,
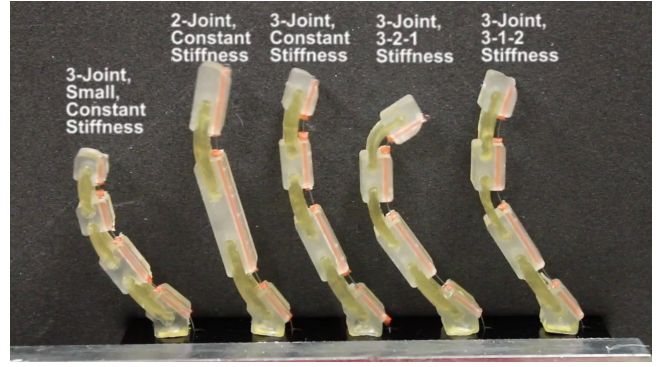

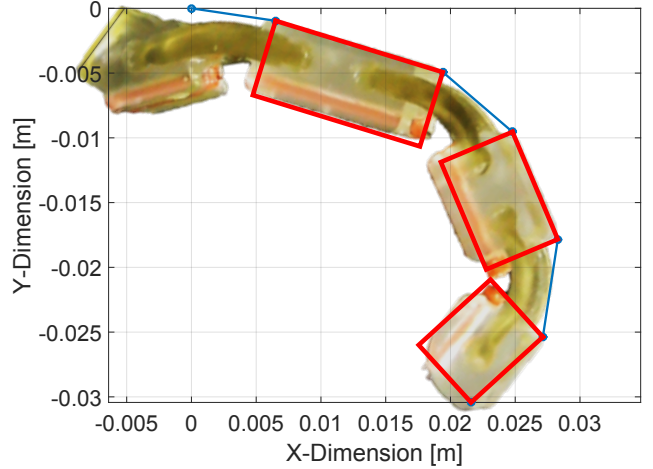Fig. 9.   Empirical finger models with varying configurations

Fig. 10.   Comparison of analytical vs. experimental SDM finger showing agreement

as well as a 'trapping score' which provides a quantitative means of comparing the geometric trapping capabilities of each finger profile. The trapping score can be formally expressed as $\left| \sum_{i=1}^{N} W_i \frac{\theta_i}{||s_i||_2} \right|$, where $||s_i||_2 = ||[l_i, \delta_i]||_2$ is Euclidean distance between subsequent segments and W_i is a shape weight. This is essentially a discretized representation of finger curvature summed over all segments, and setting $W_i \propto i$ favors distal curvature for geometric trapping. More generally, the trapping score is representative of the likelihood of a finger to trap an object and is purely based on the deformed shape of the finger with no consideration of the applied force or weight of the object. From Table 2 it is evident that configuration 1 offered the best compromise between trapping score and transmission ratio, and the measured transmission ratio (which was found by using a spring force gauge to measure the tension force required to pick up an object of known mass) closely matches that predicted by the analytical model. In addition, it was discovered that decreasing the joint stiffness from proximal to distal joints is an advantageous configuration that was pursued for the final design.

Note that this approach differs from joint stiffness optimization results in [25], which implements a distally-

Table 2. Results of empirical optimization

Config-uration	Trapping Score	Transmission Ratio	Predicted Ratio
1	23.5	13.6%	11.3%
2	15.5	10.2%	12.4%
3	25.9	9.20%	9.60%

increasing joint stiffness paradigm for grasping rigid objects in unstructured environments (with an optimum ratio of $k_2/k_1 = 0.1$ for a two-link manipulator). Dollar showed that, as an object is grasped and brought towards proximal links, the object provides a reaction force against the proximal links, thus allowing distal links to tighten around the object to achieve a stable grasp via multi-point contact. In this work, we anticipate manipulating objects with appreciable compliance, meaning we cannot rely on a grasped object to provide enough reaction force to significantly affect the grasper kinematics as the objects are enveloped. As such, we implemented the inverse approach wherein the joint stiffness decreases distally such that the distal-most joint experiences the most bending as a function of cable tension regardless of whether or not an object has been grasped.

The final finger design employed the stiffness characteristics of configuration 1 (namely, proportionally-decreasing stiffness, where the flexure joints have thicknesses of 2.65mm, 2.15mm and 1.65mm from proximal to distal) and a top-mounted cable mounting scheme, and the model was validated against an SDM prototype of the final finger design. The transmission ratio was empirically determined using a force gauge to quantify tension force, and a 6-axis load cell (ATI Nano17, Apex, NC, USA) to quantify reaction force at the distal segment. The results of the analysis are presented in Fig. 11. The measured transmission ratio is about 23%, which is very close to the theoretical value of 25% as predicted by the analytical model with a top-mounted cable scheme. Note that this scheme is twice as efficient as the direct-through scheme implemented in the empirical mod-

els, a consequence which was captured in both the analytical and empirical models.

2.3.3 Torsional Stiffness Enhancement

The flexural components of the fingers are made from a hyperelastic urethane compound, allowing for high degrees of flexion and elongation before failure. The joint compliance allows for reasonable transmission ratios, and the elastomeric behavior results in a damped response to step inputs (loading and unloading). However, due to this compliance, the torsional stiffness is quite low, and the empirical testing discussed earlier showed this compliance to be a source of grasping instability. Thus, the torsional stiffness of the joints was augmented by embedding extremely thin, precision-lasercut steel flexures into the elastomer joints. The thickness of the steel flexures was analytically optimized, as the goal was to increase the torsional stiffness while letting the elastomer to dominate the bending behavior of the joint (in other words, the presence of the steel flexure should not significantly increase the bending stiffness of the joint).

An analysis was performed in MATLAB to determine the optimum flexure thickness, as other geometric parameters (width and length) are already pre-determined by the geometric optimization results. Let us define torsional and bending stiffness enhancement factors, S_t and S_b, respectively, as:

$$S_t = \frac{\tau_s + \tau_e}{\tau_{e,0}} \tag{6}$$

$$S_b = \frac{k_s + k_e}{k_{e,0}} \tag{7}$$

Here, τ_s, τ_e, and $\tau_{e,0}$ are steel, augmented elastomer, and original elastomer torsional stiffness (respectively). The variables k_s, k_e and $k_{e,0}$ are defined similarly for bending stiffness. For a simple cantilever beam, we can express the resistance to torsion τ and resistance to bending k as follows [26]:

$$\tau = \frac{G}{l} w t^3 \left(\frac{1}{3} - 0.21 \frac{t}{w} \left(1 - \frac{t^4}{12w^4} \right) \right) \tag{8}$$

$$k = \frac{3EI}{l^3} \tag{9}$$

Here, we define G as the material shear modulus, l as the length of the flexure, w as the width, t as the thickness and I as the second moment of area.

By combining Equations (8) and (9) with Equations (6) and (7), and using geometric and material parameters for the steel and elastomer, we can construct stiffness enhancement factors which are simply quantitative measures of how much the flexural stiffness is 'enhanced' by the presence of the steel flexure. As described before, the goal is to maximize S_t while keeping S_b as close to unity as possible. A plot of S_t and S_b as functions of steel flexure thickness t_s is given in Fig. 12. The maximum flexure curvature before yield
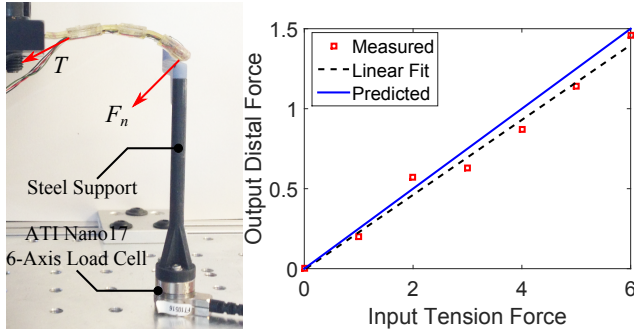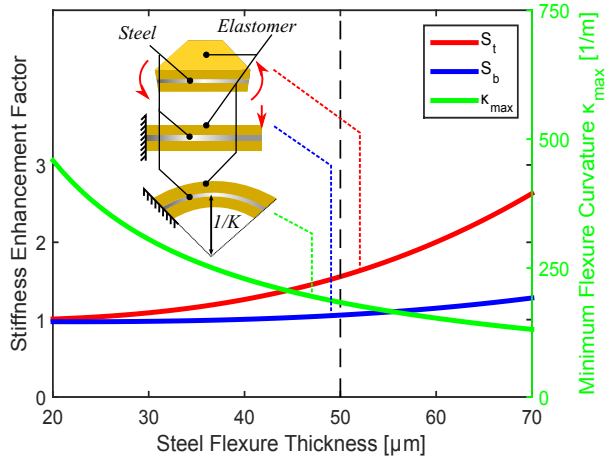

Fig. 11. (left) Experimental setup for measuring the transmission ratio, and (right) comparison of analytical vs. experimental SDM finger showing agreement

Fig. 12. Torsional stiffness enhancement analysis. For a steel flexure thickness of 50 μm, the bending stiffness of the joint remains unchanged, whereas the torsional stiffness is improved by 50%

(where $\kappa_{max} = 2\sigma_y/(Et_s)$ and σ_y is the yield stress of 304SS, taken as 210 MPa) is plotted on the secondary y-axis. At a flexure thickness of 50 μm, for the thinnest elastomer joint (1.65 mm), the bending stiffness remains relatively unaffected (S_b=1.05), whereas the torsional stiffness is improved by 50% (S_t=1.50). In addition, the maximum curvature before yield is 184 m^{-1} (corresponding to a minimum radius of 5.4 mm), meaning the finger would have to effectively fold in on itself before the flexure joints yield. As such, 0.002" steel (51 μm) was chosen to embed into the elastomer.

2.4 Pressure Sensing

In addition to the passive compliance offered by the soft, multi-jointed fingers, the grasper incorporates embedded pressure sensors in the distal segment of each finger, thus enabling active monitoring of the pressure being exerted on tissue by our device. A surface-mounted RGB LED in the handle provides a visual means of understanding the grasp-
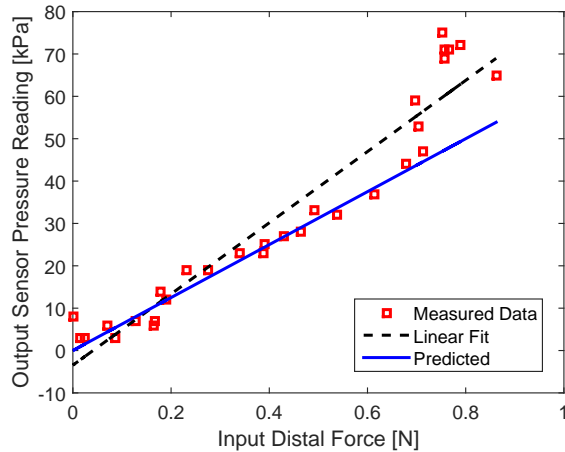

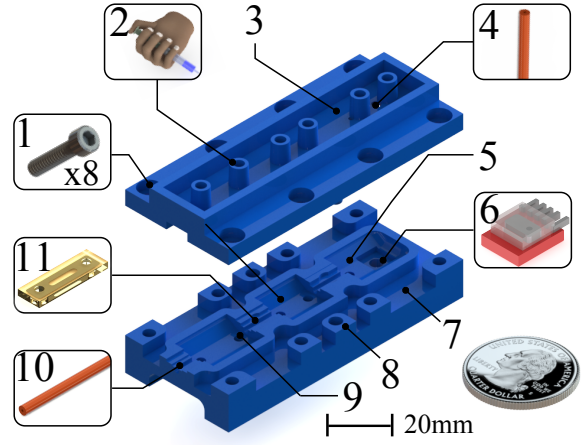Fig. 13. Calibration curve for the embedded barometric pressure sensors

Fig. 14. Closed-top mold design (US quarter for scale): (1) countersunk holes for fasteners, (2) inflow and outflow sprues/risers for polymer injection, (3) overflow basin to isolate screws from elastomer, (4) outlet for cable sheath, (5) stiff segment pocket, (6) press-fit feature for pressure sensor, (7) overflow drain, (8) alignment holes (mate with pin on underside of top mold, not shown), (9) release pin throughhole, (10) inlet for cable sheath and wiring, and (11) press-fit pocket for steel-reinforced flexible segments

ing force, where the LED turns from green to red once a pre-defined pressure threshold has been exceeded.

The sensors themselves are MEMS barometric pressure sensors encapsulated in rubber elastomer (manufactured by Takktile LLC) [27]. Sensor calibration data was obtained post-manufacturing by pressing the sensorized distal segment of a finger against a 6-axis load cell and correlating the readings. An example calibration curve is given in Fig. 13. The data is sufficiently linear, and when the pressure at each finger is averaged, we can obtain an estimate of the average grasping pressure. It should be noted that the sensor placement is arbitrary and can just as easily be implemented in all finger segments, but for a proof of concept, distal sensing alone was deemed sufficient.

2.5 Two-Part SDM Process

The basic SDM process introduced in Fig. 5 was modified to accommodate the complexities inherent in our final finger design. In particular, the complicated finger geometry required to optimize the surface area-to-volume ratio necessitated a closed mold to pattern features on all sides of the fingers. As a consequence of this, the flexible joints themselves had to be pre-molded and inserted into the final molds for encapsulation, as a closed-top mold no longer permits open-air access for subtractive machining of flexible joints. A detail of the master-mold, with call-outs to features which will be referred to in subsequent sections, is shown in Fig. 14.

2.5.1 Flexure Joint Molding

The two-part molding process is illustrated in Fig. 15. In the first SDM process, the steel-reinforced elastomer joints were molded out of PMC-780 urethane rubber compound. 0.002" thick 304 stainless steel reinforcment flexures

1. Flexure Mold   **2.** Component Placement   **3.** Mold Closure   **4.** Stiff Polymer Injection   **5**. Release Complete Fingers
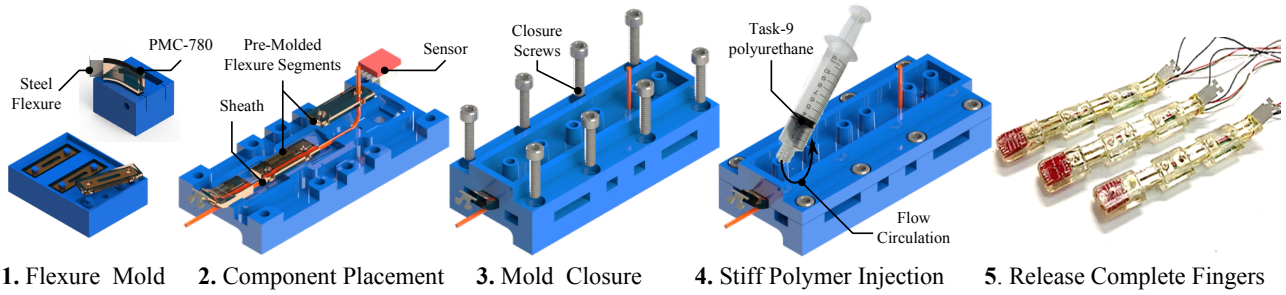
Fig. 15. Closed-Top SDM: (1) open-top molding of flexure hinges with embedded steel flexures, (2) pick-and-placement of flexures, sensors and cabling in master mold, (3) mold closure, (4) injection of Task-9 polyurethane, (5) release fingers after sufficient curing

were precision-machined using a diode-pumped solid-state (DPSS) Nd:YVO$_4$ laser, q-switched and frequency tripled to 355 nm, with a cutting speed of 20 mm/s and a frequency of 20 kHz. The steel flexures feature holes and slots (as seen in Step 1 of Fig. 15) to (1) interface with mold alignment pins and (2) allow the elastomer to flow through to 'lock in' the steel flexure. One-part, open-top molds were 3-D printed (Objet 350 Connex) with flanged alignment pins to locate the steel flexures at the neutral axis of the flexural joint. The steel flexures were placed in the mold, and the PMC-780 was poured over each mold and degassed to remove any bubbles. After a 4-hour curing time, the joints were removed from the mold and prepared for the second molding process.

2.5.2 Master Mold and Integration

The second SDM process molds the stiff structural segment, thus integrating the pre-molded steel-reinforced flexible joints, distal pressure sensor, wiring, and actuation cable sheath to realize a fully-encapsulated, fully-functional three-jointed finger. The master molds were 3D printed out of a translucent material (*VeroClear RGD810*), with alignment features to spatially locate and constrain the flexible joints, sensor, and all wiring and cabling. A thin film of mold release was applied to all molding and mating surfaces to ensure that the cured polymer would not lock the molds together. Various drains and basins are pre-designed into the mold (Fig. 14) to ensure that the polymer would not flow into screw holes. A hollow tube was placed in each finger mold to serve as a pathway for the actuation cable, which is bent upwards in the distal-most segment to realize a top-mounted cable scheme discussed previously. Inflow sprues and outflow risers over each segment provide circular paths for liquid flow, ensuring adequate filling. Components (flexible joints, sensor, wiring and cable sheath) were laid out in each mold, and gaps between mold cavities were filled in with modeling clay to prevent leakage. Each mold was tightly sealed using eight M2.5 socket-head cap screws to create a liquid-tight seal. Pre-degassed Task-9 polyurethane elastomer was injected into each segment cavity with a syringe, and injection quality was visually monitored through the transparent mold throughout the pot life of the elastomer to ensure adequate filling and absence of bubbles. After a 12-hour cure time, fingers were released from the molds and the sensors were tested.
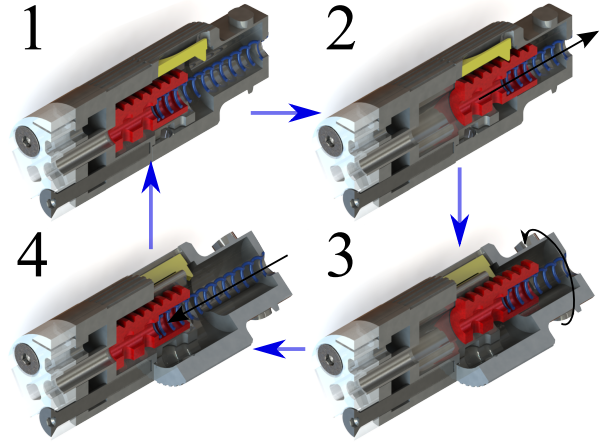

Fig. 16. Handle operation (cross-sectional isometric view), where the ratchet is shown in red, the pawl is shown in yellow and the return spring is shown in blue

2.6 Quick Release Handle Design

While the majority of this paper has focused on the design and manufacturing of the SDM fingers, the handle is also an important element of the system that required careful design to satisfy the functional requirements. The handle, which was 3D printed (Shapeways, Inc.) out of 420 stainless steel infused with bronze, was designed to hold all the fingers and electronics, interface with laparoscopic forceps, and realize the reversible locking function allowing the surgeon to quickly relieve cable tension through a 45 degree rotation. Rotation is a complicated motion compared to pinch but still relatively easy to accomplish by two laparoscopic tools. By decoupling the tensioning and release motions, the surgeon is less likely to relieve tension accidentally. However, the motion is still simple enough to release the grasper in a short amount of time as required by our functional requirements.

The lock and release mechanism functions like a reversible linear ratchet. An illustrated storyboard of the lock and release process is shown in Fig. 16. The pawl engages with the ratchet pin, to which the actuation cables for each finger are fastened. When the ratchet pin is driven by pulling the cable towards the right, tension is established uniformly in each finger, resulting in a grasping motion. The pawl prevents system backdriveability and maintains tension, so the surgeon only needs to apply short-duration bursts of force to
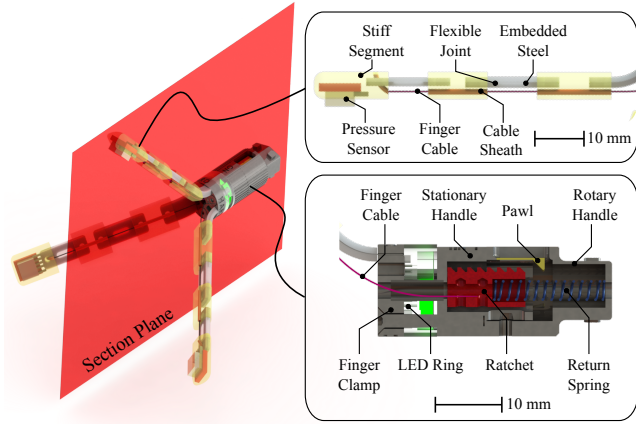
Fig. 17. Sectional view of grasper modules with callouts to important features

Fig. 18. Creep test (displacement vs. time) with a 1.5N load applied to the end of the joint in cantilever fashion (inset shows the testing setup)

develop the grasping tension incrementally. After rotating the handle by 45 degrees, the pawl and the ratchet pin disengage, and the ratchet pin is displaced to its original position by a compression spring, quickly relieving the tension in the cable and opening up the fingers for swift removal. The pawl design was optimized such that, when in combination with the required cable tension to fully close the fingers, the required pulling force is less than 10N. The proximal end of the handle features protrusions that positively engage with *Prograsp* forceps so that a stable grasp can be established.

2.7 Integration

A sectional view of the grasper, showing integrated features, is shown in Fig. 17. The proximal flexible segment of the finger has a pre-curved morphology, realizing the passive-open state. The steel flexure in this joint protrudes from the rubber, and a dogbone cutout positively engages with a feature in the handle. The finger cables are routed through a hole in the LED ring and fastened to the ratchet.

3 Validation
3.1 Creep Test

In order to ensure that creep effects of the elastomeric joints do not significantly detract from long-term device function, we performed a creep test wherein a constant load of 1.5N was applied to the end of a single steel-enhanced elastomeric joint (using an Instron tensile testing machine with a 10N load cell and a sample period of 100 ms), and the resulting deflection was monitored over a long period of time (30 minutes). The results are shown in Fig. 18, where the data has been fit to an exponential curve of the form $\delta = ae^{bt} + ce^{dt}$. It can be observed that creep effects are relatively insubstantial, affecting long-term joint deflection by a little over 10%. Further qualitative tests, wherein the fully-integrated grasper was actuated around a Nitrile glove filled with 100g of water and suspended against the glove's weight, showed that the grasper can maintain a stable grasp for over three hours. As such, we conclude that the viscoelastic properties of the joints do not substantially affect the steady-state operation of the device.
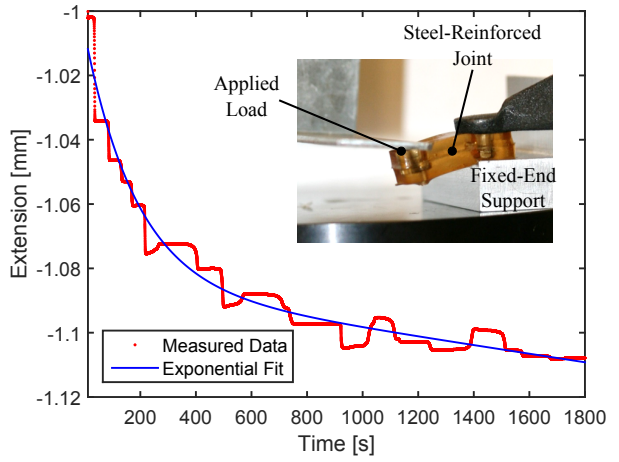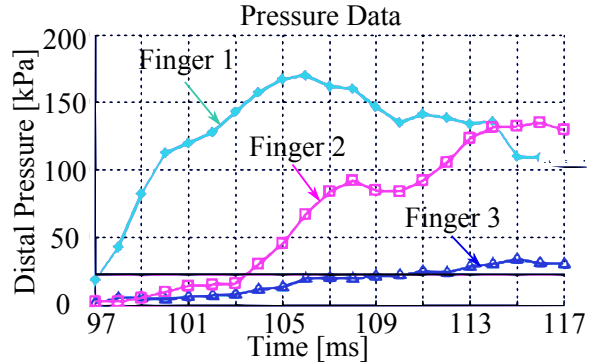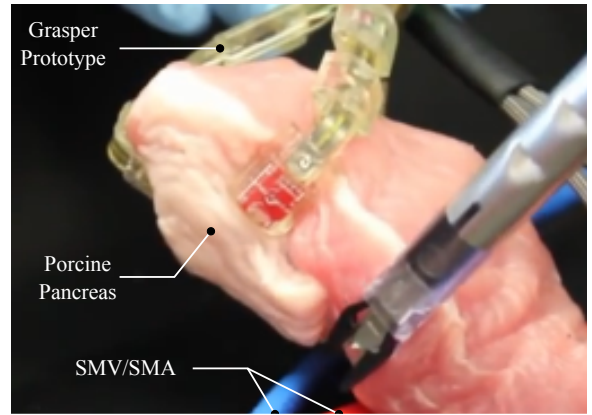

Fig. 19. (top) benchtop simulation showing the grasper prototype manipulating a porcine pancreas (weight: 80 grams), and (bottom) representative pressure profile captured during simulation

3.2 Benchtop Validation

To understand device behavior with a more accurate tissue model, we created a mock-up of an insufflated abdomen and manually positioned the grasper around a porcine pancreas (weight: 80 grams). The grasper was (1) positioned around the head of the pancreas, (2) actuated to acquire a stable grasp, and (3) elevated to retract the pancreatic head and expose the underlying anatomy. An image of the retraction task is shown in Fig. 19. Ultimately the grasper was able to conform to and deftly manipulate the porcine analog.
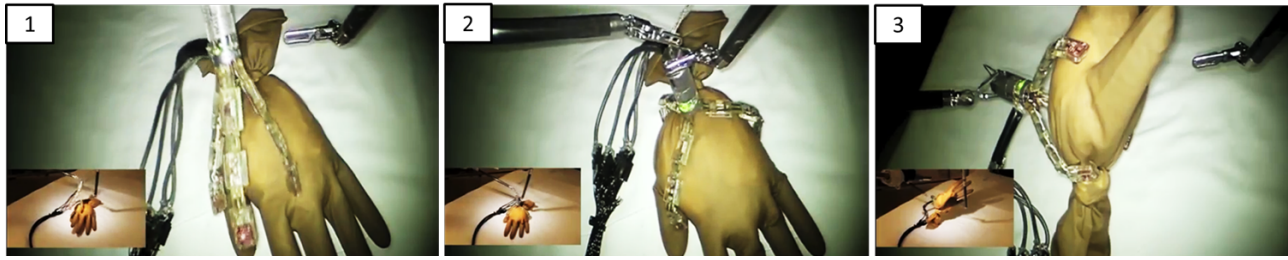
Fig. 20. daVinci simulation storyboard as seen through stereoscope (inset is external view): (1) device retrieval, (2) device positioning around pancreas analog, cable tensioning, (3) cephalad retraction

3.3 Robotic Validation

Our device was qualitatively evaluated in a simulated robotic procedure. An Intuitive *daVinci* system, equipped with one endoscope and two *Prograsp* forceps, interfaced with our device to pick up and manipulate a pancreas analog. The procedure was performed by an experienced robotic surgeon at Beth Israel Deaconess Medical Center in Boston, MA. As the experiment was performed in a sterile environment, the pancreas analog was a nitrile glove filled with tissue, gloves and other miscellaneous sterile items, and the final weight was 50g.

Overall, the results of the procedure are extremely promising. Screenshots of the simulated procedure are shown in Fig. 20. The multi-jointed, compliant nature of the deployable manipulator allowed it to passively adapt to the complicated geometry of the pancreas analog. The surgeon did not experience trouble in deftly manipulating the device and situating it onto the pancreas analog. In cases where the passive open state was not wide enough to envelope the object of interest, the surgeon was able to use the robotic forceps to assist in situating the fingers around the object. The deployable grasper was able to maintain a stable grasp once rotated 90 degrees, to simulate exposure of the posterior tributaries connecting the pancreas to the SMV/SMA.

In spite of overall success, there are a few areas for improvement which will be addressed in subsequent design iterations. It was observed that, rather than pulling the cable tension loop axially to establish tension, the surgeon instead performed a twisting motion to tension the cable, which was much more controlled. Given this preference, we will devise a mechanism which facilitates this motion to tension the cable.

The surgeon also experienced some difficulty rotating the latch to release tension. This is primarily due to the fact that there is only one area of the handle with engagement features for the *ProGrasp* to positively engage the handle. As a result, the surgeon was not able to provide a counter-torque to twist the handle. Future designs will incorporate numerous engagement features along the length of the handle to facilitate this motion.

4 Conclusions and Next Steps

We have presented the design, analyses, fabrication and testing results of a novel, deployable, atraumatic grasper for minimally invasive surgical procedures. Our device aims to eliminate the potential for intraoperative complications caused by sharp, rigid tools and the lack of haptic feedback in robotic laparoscopic surgical procedures by providing a soft interface between current tools and friable tissue. Active pressure monitoring via embedded pressure sensing provides the surgeon with visual feedback. Qualitative evaluations and robotic simulations have shown that our device is capable of being delivered through a 15mm trocar, interfacing with current laparoscopic tools, conforming to complicated and compliant geometries, and maintaining stable grasping for retraction purposes.

Future efforts will focus on further development and validation of the analytical model by analyzing finger behavior throughout the entire range of motion and at different points along the finger. The handle design will be revisited to eliminate the incidence of sharp corners and accommodate surgeon feedback, with the primary aim of reducing the size and the weight. In addition, the tensioning mechanism will be altered to accommodate the rotary tensioning technique exhibited by the surgeon during the simulation. Compact underactuation modalities will be explored to allow the fingers to exhibit unique, decoupled bending profiles for greater conformability. Alternative sensing modalities will be explored that will enable fully on-board power systems and signal conditioning. Further evaluation will be performed in the form of in vivo tests on porcine or cadaveric models.

References

[1] Zeh III, H., Bartlett, D., and Moser, A., 2011. "Robotic-assisted major pancreatic resection". *Advances in Surgery,* **45**, pp. 232–40.

[2] Dollar, A., and Howe, R., 2006. "A robust comppliant grasper via shape deposition manufacturing". *IEEE Transactions on Mechatronics,* **11**.

[3] Binnard, M., and Cutkosky, M., 2000. "A design by composition approach for layered manufacturing". *J. Mech. Design,* **122**, pp. 90–101.

[4] Merz, R., Prinz, F., Ramaswami, K., Terk, M., and Weiss, L., 1994. "Shape deposition manufacturing". *Solid Freeform Fabrication Symposium.*

[5] Guillanotti, P., Sbrana, F., Bianco, F., Elli, E., Shah, G., Addeo, P., Caravaglios, G., and Coratti, A., 2010. "Robot-assisted laparascopic pancreatic surgery: single-surgeon experience". *Surgical Endoscopy,* **24**, pp. 1646–1657.

[6] Intuitive, 2013. Intuitive surgical website. On the WWW. URL: http://www.intuitivesurgical.com/.

[7] Singer, E., 2010. The slow rise of the robotic surgeon. On the WWW, May. URL: http://www.technologyreview.com/news/418141/the-slow-rise-of-the-robot-surgeon/.

[8] Surgical, I., 2013. davinci endowrist instrument and accessory catalog.

[9] Ortiz, M., 1993. Manipulable hand for laparoscopy. US Patent, No. 5441494 A.

[10] Viola, F., 1998. Apparatus and method for performing surgical tasks during laparoscopic procedures. US Patent, No. 5807376 A.

[11] Geriffiths, J., 2001. Laparoscopic instrument with parallel actuated jaws. US Patent, No. 6238414 B1.

[12] Takayama, T., Omata, T., Futami, T., Akamatsu, H., Ohya, T., Kojima, K., Takase, K., and Tanaka, N., 2007. "Detachable-fingered hands for manipulation of large internal organs in laparoscopic surgery". *IEEE International Conference on Robotics and Automation.*

[13] Ohshima, R., Takayama, T., Omata, T., Ohya, T., Kojima, K., Takase, K., and Tanaka, N., 2009. "Assemblable three-fingered five-dof hand for laparoscopic surgery". *IEEE International Conference on Robotics and Automation.*

[14] Briscoe, R., 2010. Methods and devices for stabilizing tissue. US Patent, No. 7794387 B2.

[15] Slater, C., 1995. Endoscopic instrument with end effectors forming suction and/or irrigation lumens. US Patent, No. 5417709 A.

[16] De, S., 2008. *The Grasper-Tissue Interface in Minimally Invasive Surgery: Stress and Acute Indicators of Injury.* University of Washington.

[17] Innes, J., and Carey, L., 1994. "Normal pancreatic dimensions in the adult human". *The American Journal of Surgery,* **167**, pp. 261–263.

[18] Szczepaniak, E., Malliaras, K., Nelson, M., and Szczepaniak, L., 2013. "Measurement of pancreatic volume by abdominal mri: A validation study". *PLoS ONE,* **8**(2).

[19] Mulier, J., Dillemans, B., Crombach, M., Missant, C., and Sels, A., 2008. "On the abdominal pressure volume relationship". *The Internet Journal of Anesthesiology,* **28**(1).

[20] Dollar, A., Jentoft, L., Gao, J., and Howe, R., 2010. "Contact sensing and grasping performance of compliant hands". *Auton Robot,* **28**, pp. 65–75.

[21] Bailey, S., Cham, J., Cutkosky, R., and Full, R., 1999. "Biomimetic robotic mechanisms via shape deposition manufacturing". *ISRR.*

[22] Odhner, L., and Dollar, A., 2012. "The smooth curvature model: An efficient representation of euler-bernoulli flexures as robot joints". *IEEE Transactions on Robotics,* **28**.

[23] Budynas, R., and Nisbett, J., 2008. *Shigley's Mechanical Engineering Design.* McGraw-Hill, New York.

[24] Kanyanta, V., and Ivankovic, A., 2010. "Mechanical characterisation of polyurethane elastomer for biomedical applications". *Journal of the Mechanical Behavior of Biomedical Materials,* **3**, pp. 51–62.

[25] Dollar, A., and Howe, R., 2006. "Towards grasping in unstructured environments: Grasper compliance and configuration optimization". *Adv. Robot,* **19**(5), pp. 523–544.

[26] Young, W., and Budynas, R., 2002. *Roark's Formulas for Stress and Strain, 7th Edition.* McGraw-Hill, New York.

[27] Tenzer, Y., Jentoft, L., and Howe, R., 2012. "Inexpensive and easily customized tactile array sensors using mems barometers chips". *IEEE R and Z Magazine.*

Appendix A: Kinematics Modeling

To find the global coordinates of each subsequent section (which we will denote Δ_i for deflection in the y-direction and L_i for displacement in the x-direction), we need to add contributions from previous relative deflections due to internal moment balances and account for rotations due to the slope of the previous member. We start by attaching a local frame of reference $\{\mathbf{B}\}_i$ to the origin of segment i, where $b_{1,i}$ points along the axis of the segment and $b_{2,i}$ is the outward normal. By observing that the global orientation Θ_i of each segment is simply the sum of all local orientations $\sum_{k=1}^{i} \theta_k$, to express the local segment coordinates in the global frame, we begin by translating the local frame $\{\mathbf{B}\}_i$ to the global origin in $\{\mathbf{A}\}$, rotating by angle Θ_{i-1}, and translating back to the local origin. The sequence of transformations to map from local coordinates to global coordinates is given by the following:

$$\begin{bmatrix} L_i \\ \Delta_i \\ 1 \end{bmatrix} = \mathbf{T_1}\mathbf{R}\mathbf{T_2} \begin{bmatrix} L_{i-1}+l_i \\ \Delta_{i-1}+\delta_i \\ 1 \end{bmatrix} \qquad (10)$$

Here, $\mathbf{T_1} \in \Re^{3\times3}$ is a linear translation of (L_{i-1}, Δ_{i-1}), $\mathbf{R} \in \Re^{3\times3}$ is a rotation about Θ_{i-1} and $\mathbf{T_2} \in \Re^{3\times3}$ is a linear translation of $(-L_{i-1}, -\Delta_{i-1})$.